# Eu3+ -doped ratiometric optical thermometers: Experiment and Judd-Ofelt modelling

Kolesnikov Ilya E., Mamonova Daria V., Kurochkin Mikhail A., Kolesnikov Evgenii Yu, Lähderanta Erkki



**DOI:** 10.1016/j.optmat.2020.110797

# $Eu^{3+}$-doped ratiometric optical thermometers: experiment and Judd-Ofelt modelling

Ilya E. Kolesnikov[a,b,*], Daria V. Mamonova[a], Mikhail A. Kurochkin[a], Evgenii Yu. Kolesnikov[c], Erkki Lähderanta[b]

[a] *St. Petersburg State University, Universitetskaya nab. 7-9, 199034, St. Petersburg, Russia*
[b] *LUT University, Skinnarilankatu 34, 53850, Lappeenranta, Finland*
[c] *Volga State University of Technology, Lenin sqr. 3, 424000, Yoshkar-Ola, Russia*

## Abstract

Rare earth-doped materials are successfully utilized as non-contact optical temperature sensors. Thermal sensing is usually based on the ratiometric technique between two separate emission lines originated from thermally-coupled levels. We study $Gd_2O_3$:$Eu^{3+}$ 1 at.% and YAG: $Eu^{3+}$ 4 at.% phosphors as luminescence thermometers in 298–473 K range using both conventional experimental and Judd-Ofelt based theoretical approaches. Thermometric performances of suggested sensors were quantified through absolute and relative thermal sensitivities and temperature resolution. Experiment and theoretical modelling gave similar results. This proves the theoretical model as a simple and fast method for estimation of the $Eu^{3+}$-doped thermometer perspectives.

**Keywords:** $Eu^{3+}$, luminescence thermometry, Judd-Ofelt theory, thermally-coupled levels

## 1. Introduction

Temperature is one of the most frequently measured physical parameters as it affects almost all aspects of our lives. An accurate temperature measurement is necessary for the reliable characterization and control of processes in various fields from biology and medicine to industrial production [1–3]. Direct determining of temperature is impossible, but it can be measured via control of various characteristics of bodies such as volume, pressure, conductivity, etc. that are monotonically correlated with temperature change. The known thermal sensing methods can be divided into three groups based on the nature of contact between the sensor and the object of analysis: invasive (sensor is in direct contact with the analyzed object), semi-invasive (the object is treated to enable the remote observation) and non-invasive (remote observation) [4,5]. Last decade we have witnessed the rapid development of various semi- and non-invasive thermometry techniques due to the strong demand for accurate temperature sensing with sub-micron spatial and sub-degree thermal resolution in micro- and nanoelectronics as well as in nanomedicine [6–9]. Among these techniques, the luminescence thermometry has gained considerable interest because of its advantages of fast response and applicability in hostile environments and high electromagnetic fields [10]. Luminescence thermal sensing was successfully demonstrated using different types of phosphors including quantum dots, fluorescent dyes and proteins, polymers, metal–organic frameworks, and rare earth or transition metal-doped materials [11–18]. Rare earth-doped phosphors have attracted the most attention as optical thermometers due to their unique spectroscopic properties: narrow emission and excitation lines, long lifetime, large Stokes shift, and diversity of emitting wavelength [19,20].

Luminescence thermometry utilizes temperature-induced changes in luminescence parameters such as intensity (single band or ratiometric), spectral line position, bandwidth, lifetime, and polarization [6,21–23]. Luminescence intensity ratio (LIR) has established as the most frequently used sensing parameter thanks to intrinsic immunity to the external disturbances during the

detection process, such as the fluorescence loss, the phosphor amount, and the fluctuations of excitation intensity [24–26]. LIR is usually calculated between two separate emission lines originated from thermally coupled levels with an energy gap of 200–2000 $cm^{-1}$ [27,28].

Nowadays, a lot of scientific groups are constantly looking for new ratiometric thermometers with enhanced thermometric performances. Traditional LIR analysis requires expensive equipment, time-consuming measurements followed by a complicated data treatment [29]. Taking into account a large number of rare earth ions and potential hosts for doping, it is hard to check all these materials from the thermometric point of view via a traditional approach. To solve this problem, Ciric et al. developed an extension of the Judd-Ofelt theory to the field of lanthanide thermometry, which allows calculating thermometric performances from the single emission spectrum measured at room temperature [29]. The theoretically calculated parameters could slightly differ from the experimentally obtained ones due to imperfections of Judd-Ofelt theory and spectroscopic data acquisition and treatment. However, Ciric et al. showed the applicability of the model for the most difficult case of $Eu^{3+}$-doped $Y_2O_3$ samples, which have the largest discrepancy between theoretical and experimental parameters because of the widest energy gap among rare earth ions [29].

Herein, we checked model applicability for various $Eu^{3+}$-doped hosts as well as for different nature of emission transitions utilized for LIR calculation (including mixed electric + magnetic dipole character).

## 2. Experimental

Synthesis of $Gd_2O_3$:$Eu^{3+}$ 1 at.% particles were carried out using the combined Pechini-foaming technique, which is based on the standard Pechini method. This technique was described in detail for rare earth-doped yttrium and lutetium oxides [30,31]. The auxiliary components were added to the system during the preparation of metal polymer gel. These components provide an intensive gas release from the entire system during the pyrolysis of metal polymer gel, preventing sintering of particles. After preparing a solution of citrate complexes of metals, potassium carbonate was added to the system, which filled the cells of polymer gel. The gel was calcinated at 1000 $^oC$ for 1 hour to remove organic components. The prepared particles were collected by centrifugation at 2800 rpm for 5 min repeated 3 times. The resulting washed precipitate was dried in an oven at 110 $^oC$.

Nanocrystalline $Y_3Al_5O_{12}$:$Eu^{3+}$ 4 at.% (YAG:$Eu^{3+}$ 4 at.%) sample was prepared using the modified Pechini method based on additional heat treatment of the amorphous precursor in a molten salt [32]. Briefly, the citrate complexes of **$Y^{3+}$, $Eu^{3+}$ and $Al^{3+}$** are crosslinked with ethylene glycol to form a polymer gel, which was then calcinated at 850 $^oC$ for two hours. The obtained amorphous substance was held in the molten KCl at 1000 $^oC$ for one hour under an ambient atmosphere. The residual salt is removed from the system by washing in distilled water three times. The synthesized particles were collected by centrifugation (2800 rpm for 5 min repeated 3 times) and then were dried in an oven at 110 $^oC$.

X-ray diffraction patterns were measured with Rigaku «Miniflex II» diffractometer with $CuK_\alpha$-radiation ($\lambda$ = 1.5406 Å) in the $2\theta$ range from 15$^o$ to 80$^o$. Phase identification was performed using a powder diffraction database PowderDiffractionFile (PDF-2, 2011). Scanning electron micrograph (SEM) images were obtained using SUPRA 40VP WDS scanning electron microscope. Emission spectra were measured on modular fluorescence spectrometer Fluorolog-3 with diode laser CUBE (Coherent) 384 nm as an excitation source. Temperature experiments were carried out on the same spectrometer equipped with optical fibers and heating stage Linkam

THMS 600 with a resolution of 0.1 °C. During temperature experiments, a 5 min waiting time was used to achieve the steady-state temperature regime before measuring. **Different $Eu^{3+}$ doping concentration in $Gd_2O_3$ and $Y_3Al_5O_{12}$ hosts was used to study its effect on temperature calibration curve.**

## 3. Results and discussion

The phase composition of the synthesized $Eu^{3+}$-doped sample was studied using X-ray Powder Diffraction. XRD pattern of synthesized $Gd_2O_3$:$Eu^{3+}$ 1 at.% NPs is presented in Fig. 1a. The measured diffraction pattern displayed a good match with the standard card of $Gd_2O_3$ (ICDD 01-080-6921, space group Ia-3). No impurity line was detected. That means formation of a single phase sample. As $Eu^{3+}$ and $Gd^{3+}$ ions have very close ionic radii (109 and 108 pm, respectively), doping ions locate at gadolinium positions in the host, so the partial substitution does not affect the cubic structure. SEM image of $Gd_2O_3$:$Eu^{3+}$ 1 at.% sample, shown in Fig. 1b, displays presence particles with diameter of 80–150 nm.

Fig. 1c shows emission spectrum of $Gd_2O_3$:$Eu^{3+}$ 1 at.% NPs measured in the spectral range of 500–750 nm upon 384 nm excitation. The used excitation wavelength corresponds to $^7F_0$–$^5L_7$ transition in the europium ions [33]. The obtained spectrum consists of 4f intra-configurational transitions from metastable $^5D_0$ to lower lying $^7F_J$ levels: $^5D_0$–$^7F_0$ (580 nm), $^5D_0$–$^7F_1$ (588, 592.5, 595, 599 nm), $^5D_0$–$^7F_2$ (611.5, 613.5, 629.5 nm), $^5D_0$–$^7F_3$ (651, 653, 657, 661 nm), $^5D_0$–$^7F_4$ (687, 693, 699.5, 706.5, 708, 711 nm) [34]. Besides luminescence bands originated from $^5D_0$ level, the weak intense $^5D_1$–$^7F_1$ transition (533.5 and 537.5 nm) was also observed. One can see that emission spectrum is dominated by the forced electric dipole $^5D_0$–$^7F_2$ transition, while the magnetic dipole $^5D_0$–$^7F_1$ transition displays lower intensity.

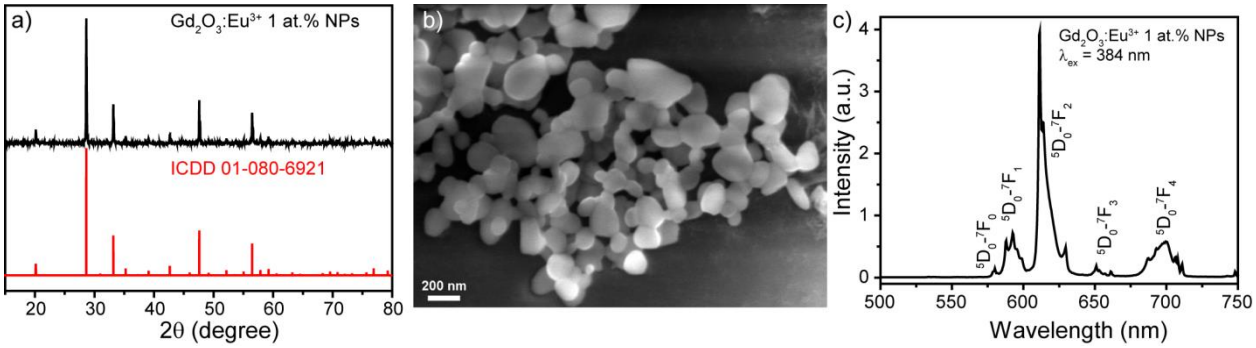


Fig. 1. a) XRD pattern of $Gd_2O_3$:$Eu^{3+}$ 1 at.% NPs with $Gd_2O_3$ standard card (ICDD 01-080-6921); b) SEM image of $Gd_2O_3$:$Eu^{3+}$ 1 at.% sample; c) room temperature emission spectrum of $Gd_2O_3$:$Eu^{3+}$ 1 at.% NPs ($\lambda_{ex}$ = 384 nm).

The presence of emission bands originated from two excited thermally coupled levels $^5D_1$ and $^5D_0$ makes $Gd_2O_3$:$Eu^{3+}$ 1 at.% NPs suitable to provide luminescence thermal sensing using the ratiometric approach. Luminescence intensity ratio (LIR) between $^5D_1$–$^7F_1$ and $^5D_0$–$^7F_1$ emission bands can serve as a temperature-dependent parameter. Taking into account the thermal coupling of $^5D_1$ and $^5D_0$ levels, LIR behavior should be governed by Boltzmann function [35,36]. Fig. 2a presents emission spectra measured at different temperatures in the range of 298–473 K. One can see that temperature increase leads to gradual growth of $^5D_1$–$^7F_1$ transition intensity, whereas $^5D_0$–$^7F_1$ transition intensity demonstrates monotonic decline. Such behavior is explained by a thermally induced population of $^5D_1$ level. LIR was calculated using integral intensities as this approach allows to provide better thermometric characteristics [37]. The spectral limits of the

integrated emission were 528–546 nm and 583–602 nm for $^5D_1$–$^7F_1$ and $^5D_0$–$^7F_1$ transitions, respectively. The temperature dependence of LIR is shown in Fig. 2b. **The experimental data are accurately fitted by an offset–corrected Boltzmann model with adj. $R^2$ better than 0.999**.

$$LIR = \frac{I_{5D1}}{I_{5D0}} = B\exp\left(-\frac{\Delta E}{kT}\right) + C \quad (1)$$

where B and C are temperature independent constants, ΔE is the energy gap between the two thermally coupled levels, and k=0.695 $cm^{-1}$ $K^{-1}$ is the Boltzmann constant. **The offset term is most probably a consequence of kinetically induced failure of Boltzmann behavior and thus, thermal decoupling of the $^5D_1$ and $^5D_0$ levels. This issue was covered in detail in recently published papers [9,38].**

Thermometric characteristics of synthesized NPs were estimated by a set of parameters: the absolute ($S_a$) and relative ($S_r$) thermal sensitivity, and the temperature resolution (δT). The absolute thermal sensitivity defines the absolute LIR change with temperature variation: $S_a = \frac{dLIR}{dT}$. It depends on absolute LIR value, which can be affected by the manipulating calculation procedure, for example, change of spectral limits for calculation of the integral intensity of emission transition. To compare the thermometers of different nature, the relative thermal sensitivity $S_r = \frac{1}{LIR}\frac{dLIR}{dT}$, which reflects the normalized change in LIR with temperature variation was introduced. The evolution of the $S_r$ and $S_a$ values with temperature is presented in Fig. 2c. One can see that the absolute thermal sensitivity monotonically increases along with temperature, while the relative sensitivity achieves a maximal value of 1.1 % $K^{-1}$ at 398 K. The temperature resolution shows the accuracy of the thermal sensing using regarded material. δT can be obtained in several ways: from the calibration curve, from the acquisition of several consecutive emission spectra at a fixed temperature, and from analysis of the thermal relaxation process [37]. Here, the temperature resolution was calculated via the first approach: $\delta T = \frac{1}{S_r}\frac{\delta LIR}{LIR}$, where δLIR/LIR is the relative uncertainty in the determination of the temperature obtained as a dispersion of three repeated measurements. δT of $Gd_2O_3$:$Eu^{3+}$ 1 at.% NPs was found to be 0.8 K at room temperature. **Noteworthy, the temperature resolution depends on the measurement setup and is strongly affected by the signal-to-noise ratio of the emission spectrum used for LIR calculation** [3]. **More precise estimation of minimal δT requires the acquisition of a larger number of emission spectra.**

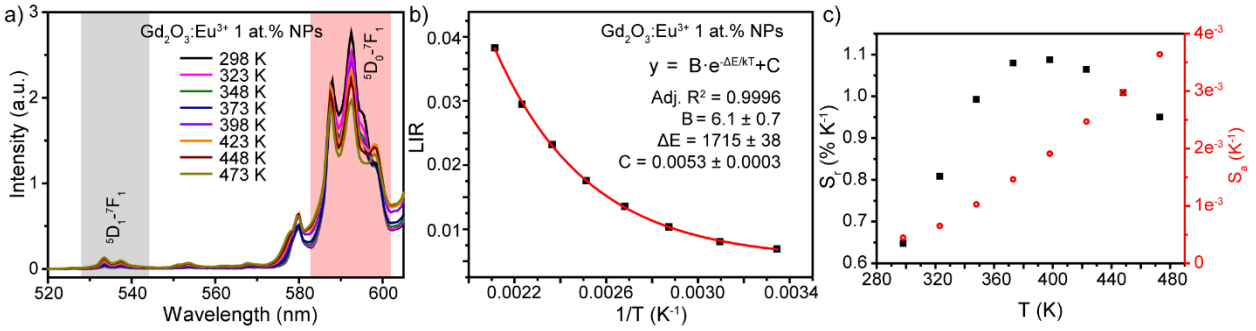


Fig. 2. a) Emission spectra of $Gd_2O_3$:$Eu^{3+}$ 1 at.% NPs obtained at different temperatures; b) LIR temperature evolution; c) temperature dependence of absolute and relative thermal sensitivities.

Fig. 3a presents XRD patterns of the prepared YAG:$Eu^{3+}$ 4 at.% powder with standard card of cubic YAG (JCPDS 33-0040, space group Ia-3d). All observed peaks coincide with the reference cubic phase with no impurity lines detected. SEM image of YAG:$Eu^{3+}$ 4 at.% NPs, presented in

Fig. 3b, shows that powder consists of particles with diameter up to 200 nm, while the average size is about 100 nm.

The emission spectrum of YAG:$Eu^{3+}$ 4 at.% NPs measured in the spectral range of 500–750 nm upon 384 nm excitation is presented in Fig. 3c. It includes characteristic narrow bands corresponding to the following transitions: $^5D_0$–$^7F_1$ (590.5 and 596 nm), $^5D_0$–$^7F_2$ (609.5, 625.5, 630, 635 nm), $^5D_0$–$^7F_3$ (649.5 and 655.5 nm), $^5D_0$–$^7F_4$ (696, 700.5, 710, 715 nm), and $^5D_0$–$^7F_5$ (743.5 and 748 nm) [39]. The most prominent transition is the forced electric dipole $^5D_0$–$^7F_4$ transition, whereas magnetic dipole $^5D_0$–$^7F_1$ transition prevails over forced electric dipole $^5D_0$–$^7F_2$ transition. Similar to $Gd_2O_3$:$Eu^{3+}$ 1 at.% NPs, it was observed a low intense line originated from higher excited $^5D_1$ level: $^5D_1$–$^7F_2$ transition (550.5 nm).

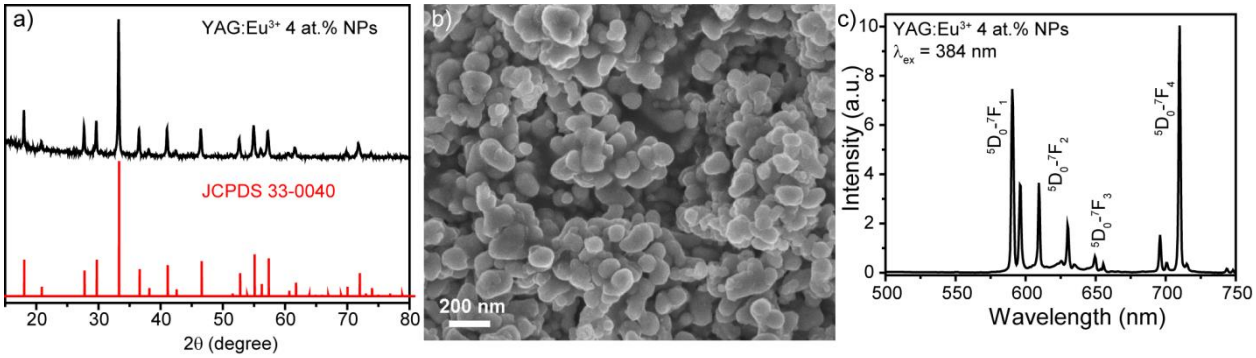


Fig. 3. a) XRD pattern of YAG:$Eu^{3+}$ 4 at.% NPs with YAG standard card (JCPDS 33-0040); b) SEM image of YAG:$Eu^{3+}$ 4 at.% sample; c) room temperature emission spectrum of YAG:$Eu^{3+}$ 4 at.% NPs ($\lambda_{ex}$ = 384 nm).

Fig. 4a shows the emission spectra of YAG:$Eu^{3+}$ 4 at.% NPs obtained at different temperatures from 298 to 473 K. The same situation as in the case of $Gd_2O_3$:$Eu^{3+}$ 1 at.% NPs was observed: the growth of temperature results in the increase of $^5D_1$–$^7F_2$ transition intensity along with the decrease of $^5D_0$–$^7F_1$ transition intensity. The total emission intensities of $^5D_1$–$^7F_2$ and $^5D_0$–$^7F_1$ transitions were obtained by integrating within 547–554 nm and 584–600 nm spectral limits, respectively. The evolution of LIR vs 1/T is presented in Fig. 4b. Equation (1) fitted the experimental points with good accuracy of Adj. $R^2$ = 0.998. Fig. 4c displays the temperature dependence of absolute and relative thermal sensitivities. One can see the gradual growth of $S_a$ value, while $S_r$ demonstrates a maximum of 1.0 % $K^{-1}$ at 423 K. The temperature resolution of YAG:$Eu^{3+}$ 4 at.% NPs was determined to be 2.7 K at 298 K.

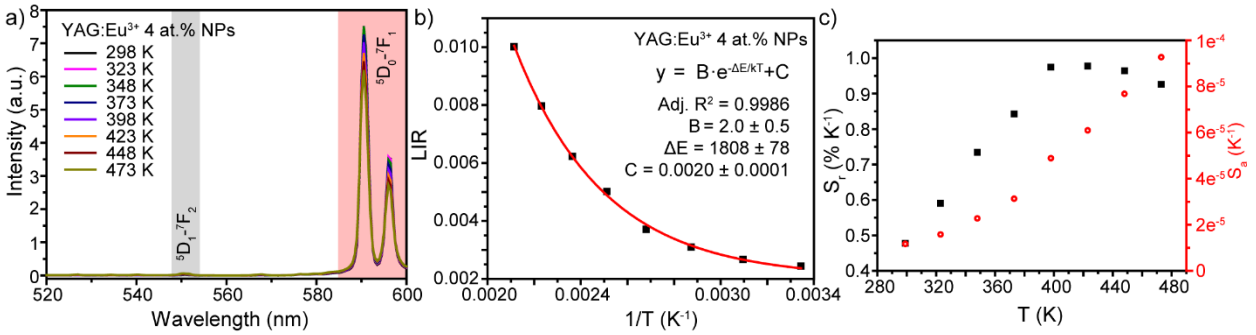


Fig. 4. a) Emission spectra of YAG:$Eu^{3+}$ 4 at.% NPs obtained at different temperatures; b) LIR temperature evolution; c) temperature dependence of absolute and relative thermal sensitivities.

Recently, Ćirić, et al. reported that LIR values and thermometric characteristics of rare earth-doped thermal sensors can be calculated using the theoretical model, which is an extension of the

Judd-Ofelt theory [29]. The B parameter in Eq. (1) can be written using the Judd-Ofelt parameters, together with the approximately host-independent magnetic dipole strength values [38]:

$$B = \left(\frac{\nu_H}{\nu_L}\right)^3 \frac{\chi_{ED}^H D_{ED}^H + \chi_{MD}^H D_{MD}^H}{\chi_{ED}^L D_{ED}^L + \chi_{MD}^L D_{MD}^L} \quad (2)$$

where H and L mean transitions from high and low energy levels, ED and MD are electric and magnetic dipole transitions, ν is the transition barycenter energy, χ is the local field correction, $D_{ED}$ and $D_{MD}$ are ED and MD strengths. **Noteworthy, the factor $\left(\frac{\nu_H}{\nu_L}\right)^3$ should be used if single photon counting detection such as in a photomultiplier tube is performed, whereas the factor $\left(\frac{\nu_H}{\nu_L}\right)^4$ is correct in case of intensity measurements are performed in terms of incident power densities.** The local field correction for ED-induced emission is $\chi_{ED} = \frac{n(n^2+2)^2}{9}$, while for the case of MD transition $\chi_{MD} = n^3$, where $n$ is refractive index at transition wavelength.

The application of this model to the case of $Eu^{3+}$-doped $Gd_2O_3$ and YAG NPs and comparison of the theoretical and experimental results are reported below. Ratiometric thermometry of $Gd_2O_3$:$Eu^{3+}$ 1 at.% NPs is based on LIR between $^5D_1$–$^7F_1$ (H) and $^5D_0$–$^7F_1$ (L) transitions. $^5D_1$–$^7F_1$ is ED transition with $\chi_{ED}^H D_{ED}^H + \chi_{MD}^H D_{MD}^H = \frac{n(n^2+2)^2}{9} \cdot 0.0026\Omega_2$. $^5D_0$–$^7F_1$ is a purely magnetic transition with $\chi_{ED}^L D_{ED}^L + \chi_{MD}^L D_{MD}^L = n^3 \cdot 9.6 \cdot 10^{-42}$. In the case of YAG:$Eu^{3+}$ 4 at.% NPs LIR was calculated using $^5D_1$–$^7F_2$ (H) and $^5D_0$–$^7F_1$ (L) transitions. $^5D_1$–$^7F_2$ transition has ED+MD character with $\chi_{ED}^H D_{ED}^H + \chi_{MD}^H D_{MD}^H = \frac{n(n^2+2)^2}{9} \cdot 0.0008\Omega_2 + n^3 \cdot 11.2 \cdot 10^{-42}$. Refractive indices of $Gd_2O_3$ and YAG were taken from [40] and [41], respectively. Judd-Ofelt parameters and barycenter of emission transitions of $Eu^{3+}$-doped NPs were obtained from room temperature emission spectra (Fig. 1c and 3c) using JOES software [42]. The values obtained using experimental and theoretical approaches are listed in Table 1. $B_{exp}$ and $\Delta E_{exp}$ were taken from temperature calibration curves (Fig. 2b and 4b). $B_{th}$ was calculated using Eq. (2), $\Delta E_{th}$ was obtained as difference between high and low energy level positions: $\Delta E_{th} = \nu_H - \nu_L$. One can see that $B_{th}$ and $B_{exp}$ display similar values taking into account that both methods carry experimental and theoretical errors. The same situation was observed for the determination of the energy gap between high and low excited levels.

Table 1. Spectroscopic and Judd-Ofelt parameters with comparison between experimentally and theoretically obtained B and ΔE values for $Gd_2O_3$:$Eu^{3+}$ 1 at.% and YAG:$Eu^{3+}$ 4 at.% NPs.

| $n_H$ | $n_L$ | $\nu_H$ | $\nu_L$ | $\Omega_2 \cdot 10^{-20}$, $cm^2$ | $\Omega_4 \cdot 10^{-20}$, $cm^2$ | $B_{th}$ | $B_{exp}$ | $\Delta E_{th}$, $cm^{-1}$ | $\Delta E_{exp}$, $cm^{-1}$ |
|---|---|---|---|---|---|---|---|---|---|
| **$Gd_2O_3$:$Eu^{3+}$ 1 at.% NPs** | | | | | | | | | |
| 2.065 | 2.0753 | 18692 | 16867 | 6.07 | 5.11 | 5.19 | 6.1 | 1825 | 1715 |
| **YAG:$Eu^{3+}$ 4 at.% NPs** | | | | | | | | | |
| 1.8361 | 1.8323 | 18149 | 16872 | 1.24 | 3.76 | 1.72 | 2.0 | 1990 | 1808 |

Thermometric performances and calibration curve can be constructed based on theoretically calculated $B_{th}$ and $\Delta E_{th}$ values. Ideally LIR behavior should be described by Boltzmann function without offset: $LIR_{th} = B_{th} \exp\left(-\frac{\Delta E_{th}}{kT}\right)$. The relative thermal sensitivity depends solely on the energy gap between thermally-coupled energy levels and equals $S_r = \frac{\Delta E_{th}}{kT^2}$, while the absolute

thermal sensitivity is expressed as follows: $S_a = \frac{\Delta E_{th}}{kT^2} \cdot B_{th} \exp\left(-\frac{\Delta E_{th}}{kT}\right)$. Presence of offset in the temperature calibration curve may be caused by overlapping peaks and stray light, and it degraded thermometric performance of sensor [5]. Thus, theoretical $B_{th}$ and $\Delta E_{th}$ values allows to calculate maximum achievable thermal sensitivities for the luminescence thermometer and access its perspective. For example, relative thermal sensitivities of 1.7 % $K^{-1}$@398K and 1.6 % $K^{-1}$@423K were found for $Gd_2O_3$:$Eu^{3+}$ 1 at.% and YAG:$Eu^{3+}$ 4 at.% NPs, respectively, which are higher compared with the experimentally obtained values.

## 4. Conclusion

$Eu^{3+}$-doped $Gd_2O_3$ and YAG phosphors were successfully synthesized via different modifications of standard Pechini technique. The applied synthesis methods allowed to obtain single phase weakly-agglomerated NPs. Emission spectra of studied samples consist of characteristic narrow lines attributed to the transitions from $^5D_1$ and $^5D_0$ excited levels to the lower $^7F_J$ levels. The presence of emission bands originated from different excited levels with the energy gap not exceeding 2000 $cm^{-1}$ makes it possible to provide ratiometric luminescence thermal sensing **for moderate temperatures**. Temperature was determined within a range of 298–473 K using LIR values. Thermometric performances of suggested temperature sensors were estimated in terms of absolute and relative thermal sensitivities as well as temperature resolution. $Gd_2O_3$:$Eu^{3+}$ 1 at.% NPs demonstrated the maximum relative sensitivity $S_r$ of 1.1 % $K^{-1}$@398K and temperature resolution δT of 0.8 K@298K, while YAG:$Eu^{3+}$ 4 at.% NPs presented $S_r$ = 1.0 % $K^{-1}$@423K and δT = 2.7 K@298K, respectively. **The theoretical model using Judd-Ofelt parameters was successfully tested on $Gd_2O_3$:$Eu^{3+}$ 1 at.% and YAG:$Eu^{3+}$ 4 at.% NPs as a tool for preliminary choice of a host material for constructing $Eu^{3+}$-doped thermometers.** Theoretically and experimentally obtained values are in a quite good agreement, demonstrating the possible application of the theoretical model for simple and fast estimation of certain ratiometric $Eu^{3+}$-doped thermal sensor perspective.


## Acknowledgments

Synthesis of samples was partially supported by the Russian Science Foundation, project № 20-79-00101. Experimental measurements were performed in “Center for Optical and Laser materials research”, “Research Centre for X-ray Diffraction Studies”, “Interdisciplinary Resource Center for Nanotechnology” (St. Petersburg State University).


## References


[1] I. Kolesnikov, D. Mamonova, A. Kalinichev, M. Kurochkin, V. Medvedev, E. Kolesnikov, et al., Constructing of efficient dual activating ratiometric YVO4: Nd3+/Eu3+ nanothermometers using co-doped and mixed phosphors, Nanoscale. 12 (2020) 5953.

[2] J. Zhong, D. Chen, Y. Peng, Y. Lu, X. Chen, X. Li, et al., A review on nanostructured glass ceramics for promising application in optical thermometry, J. Alloys Compd. 763 (2018) 34–48.

[3] A. Bednarkiewicz, L. Marciniak, L.D. Carlos, D. Jaque, Standardizing luminescence nanothermometry for biomedical applications, Nanoscale. 12 (2020) 14405–14421.

[4] P.R.N. Childs, J.R. Greenwood, C.A. Long, Review of temperature measurement, Rev. Sci. Instrum. 71 (2000) 2959–2978.

[5] C.D.S. Brites, A. Millán, L.D. Carlos, Lanthanides in Luminescent Thermometry, Handb. Phys. Chem. Rare Earths. 49 (2016) 339–427. doi:10.1016/bs.hpcre.2016.03.005.

[6] M.D. Dramićanin, Trends in luminescence thermometry, J. Appl. Phys. 128 (2020) 40902.
[7] R.G. Geitenbeek, J.C. Vollenbroek, H.M.H. Weijgertze, C.B.M. Tregouet, A.-E. Nieuwelink, C.L. Kennedy, et al., Luminescence thermometry for in situ temperature measurements in microfluidic devices, Lab Chip. 19 (2019) 1236–1246.
[8] J. Zhou, B. Del Rosal, D. Jaque, S. Uchiyama, D. Jin, Advances and challenges for fluorescence nanothermometry, Nat. Methods. 17 (2020) 967–980.
[9] R.G. Geitenbeek, H.W. de Wijn, A. Meijerink, Non-Boltzmann Luminescence in Na Y F 4: Eu 3+: Implications for Luminescence Thermometry, Phys. Rev. Appl. 10 (2018) 64006.
[10] X. Wang, O.S. Wolfbeis, R.J. Meier, Luminescent probes and sensors for temperature, Chem. Soc. Rev. 42 (2013) 7834–7869.
[11] C.D.S. Brites, P.P. Lima, N.J.O. Silva, A. Millán, V.S. Amaral, F. Palacio, et al., Lanthanide-based luminescent molecular thermometers, New J. Chem. 35 (2011) 1177–1183. doi:10.1039/c0nj01010c.
[12] C.D.S. Brites, P.P. Lima, N.J.O. Silva, A. Millán, V.S. Amaral, F. Palacio, et al., Thermometry at the nanoscale, Nanoscale. 4 (2012) 4799–4829. doi:10.1039/c2nr30663h.
[13] Y. Cui, F. Zhu, B. Chen, G. Qian, Metal–organic frameworks for luminescence thermometry, Chem. Commun. 51 (2015) 7420–7431.
[14] I.E. Kolesnikov, A.A. Kalinichev, M.A. Kurochkin, E.Y. Kolesnikov, E. Lähderanta, Porphyrins as efficient ratiometric and lifetime-based contactless optical thermometers, Mater. Des. 184 (2019) 108188.
[15] R. Marin, A. Vivian, A. Skripka, A. Migliori, V. Morandi, F. Enrichi, et al., Mercaptosilane-Passivated CuInS2 Quantum Dots for Luminescence Thermometry and Luminescent Labels, ACS Appl. Nano Mater. 2 (2019) 2426–2436.
[16] C. Matuszewska, L. Marciniak, The influence of host material on NIR II and NIR III emitting Ni2+-based luminescent thermometers in ATiO3: Ni2+ (A= Sr, Ca, Mg, Ba) nanocrystals, J. Lumin. (2020) 117221.
[17] B. del Rosal, D. Ruiz, I. Chaves-Coira, B.H. Juárez, L. Monge, G. Hong, et al., In vivo contactless brain nanothermometry, Adv. Funct. Mater. 28 (2018) 1806088.
[18] I.E. Kolesnikov, A.A. Kalinichev, M.A. Kurochkin, D.V. Mamonova, E.Y. Kolesnikov, E. Lähderanta, Ratiometric Optical Thermometry Based on Emission and Excitation Spectra of YVO <inf>4</inf> :Eu $^{3+}$ Nanophosphors, J. Phys. Chem. C. (2019). doi:10.1021/acs.jpcc.9b00284.
[19] P. Huang, W. Zheng, Z. Gong, W. You, J. Wei, X. Chen, Rare earth ion–and transition metal ion–doped inorganic luminescent nanocrystals: from fundamentals to biodetection, Mater. Today Nano. 5 (2019) 100031.
[20] X. Wang, T. Xu, P. Cai, T. Vu, H.J. Seo, Controlled synthesis, multicolor luminescence, and optical thermometer of bifunctional NaYbF4: Nd3+@ NaYF4: Yb3+ active-core/active-shell colloidal nanoparticles, J. Alloys Compd. 691 (2017) 530–536.
[21] D. Jaque, F. Vetrone, Luminescence nanothermometry, Nanoscale. 4 (2012) 4301. doi:10.1039/c2nr30764b.
[22] S. Wang, S. Westcott, W. Chen, Nanoparticle luminescence thermometry, J. Phys. Chem. B. 106 (2002) 11203–11209.
[23] I.E. Kolesnikov, A.A. Kalinichev, M.A. Kurochkin, D. V. Mamonova, E.Y. Kolesnikov, E. Lähderanta, et al., Bifunctional heater-thermometer Nd 3+ -doped nanoparticles with multiple temperature sensing parameters, Nanotechnology. 30 (2019) 145501. doi:10.1088/1361-6528/aafcb8.
[24] A.A. Kalinichev, M.A. Kurochkin, E.V. Golyeva, A.V. Kurochkin, E. Lähderanta, M.D. Mikhailov, et al., Near-infrared emitting YVO4:Nd3+nanoparticles for high sensitive fluorescence thermometry, J. Lumin. 195 (2018) 61–66. doi:10.1016/j.jlumin.2017.11.024.
[25] S.A. Wade, S.F. Collins, G.W. Baxter, Fluorescence intensity ratio technique for optical

fiber point temperature sensing, J. Appl. Phys. 94 (2003) 4743–4756.
[26] S. Zhou, X. Li, X. Wei, C. Duan, M. Yin, A new mechanism for temperature sensing based on the thermal population of 7F2 state in Eu3+, Sensors Actuators B Chem. 231 (2016) 641–645. doi:10.1016/j.snb.2016.03.082.
[27] V.K. Rai, Temperature sensors and optical sensors, Appl. Phys. B Lasers Opt. 88 (2007) 297–303. doi:10.1007/s00340-007-2717-4.
[28] Z. Sun, M. Jia, Y. Wei, J. Cheng, T. Sheng, Z. Fu, Constructing new thermally coupled levels based on different emitting centers for high sensitive optical thermometer, Chem. Eng. J. 381 (2020) 122654.
[29] A. Ćirić, S. Stojadinović, M.D. Dramićanin, An extension of the Judd-Ofelt theory to the field of lanthanide thermometry, J. Lumin. 216 (2019) 116749.
[30] I.E. Kolesnikov, D.V. Mamonova, E. Lähderanta, A.V. Kurochkin, M.D. Mikhailov, The impact of doping concentration on structure and photoluminescence of Lu2O3:Eu3+ nanocrystals, J. Lumin. 187 (2017) 26–32. doi:10.1016/j.jlumin.2017.03.006.
[31] I.E. Kolesnikov, A.A. Kalinichev, M.A. Kurochkin, D.V. Mamonova, E.Y. Kolesnikov, A.V. Kurochkin, et al., Y2O3:Nd3+ nanocrystals as ratiometric luminescence thermal sensors operating in the optical windows of biological tissues, J. Lumin. 204 (2018) 506–512. doi:10.1016/j.jlumin.2018.08.050.
[32] I.E. Kolesnikov, A. V Povolotskiy, D. V Tolstikova, A.A. Manshina, M.D. Mikhailov, Luminescence of Y3Al5O12:Eu3+ nanophosphors in blood and organic media, J. Phys. D. Appl. Phys. 48 (2015) 075401. doi:10.1088/0022-3727/48/7/075401.
[33] I. Kolesnikov, A. Povolotskiy, D. Mamonova, E. Lahderanta, A. Manshina, M. Mikhailov, Photoluminescence Properties of Eu3+ Ions in Yttrium Oxide Nanoparticles: Defect vs Normal Sites, RSC Adv. 6 (2016) 76533–76541. doi:10.1039/C6RA16814K.
[34] R. Priya, O.P. Pandey, Photoluminescent enhancement with co-doped alkali metals in Gd2O3: Eu synthesized by co-precipitation method and Judd Ofelt analysis, J. Lumin. 212 (2019) 342–353.
[35] S.F. Collins, G.W. Baxter, S.A. Wade, T. Sun, K.T. V Grattan, Z.Y. Zhang, et al., Comparison of fluorescence-based temperature sensor schemes: theoretical analysis and experimental validation, J. Appl. Phys. 84 (1998) 4649–4654.
[36] M.G. Nikolić, D.J. Jovanović, M.D. Dramićanin, Temperature dependence of emission and lifetime in Eu 3+-and Dy 3+-doped GdVO 4, Appl. Opt. 52 (2013) 1716–1724.
[37] I.E. Kolesnikov, A.A. Kalinichev, M.A. Kurochkin, D.V. Mamonova, E.Y. Kolesnikov, A.V. Kurochkin, et al., New strategy for thermal sensitivity enhancement of Nd 3+ -based ratiometric luminescence thermometers, J. Lumin. 192 (2017) 40–46. doi:10.1016/j.jlumin.2017.06.024.
[38] M. Suta, A. Meijerink, A theoretical framework for ratiometric single ion luminescent thermometers—thermodynamic and kinetic guidelines for optimized performance, Adv. Theory Simulations. (2020) 2000176.
[39] R. Han, L. Wang, K. Chen, S. Yang, Photoluminescence properties of Y3Al5O12: Eu nanocrystallites prepared by co-precipitation method using a mixed precipitator of NH4 HCO3 and NH3·H2O, Mater. Sci. Eng. B. 166 (2010) 41–45. doi:10.1016/j.mseb.2009.09.027.
[40] L. Liu, X. Chen, Energy levels, fluorescence lifetime and Judd–Ofelt parameters of Eu3+ in Gd2O3 nanocrystals, Nanotechnology. 18 (2007) 255704. doi:10.1088/0957-4484/18/25/255704.
[41] D.E. Zelmon, D.L. Small, R. Page, Refractive-index measurements of undoped yttrium aluminum garnet from 0.4 to 5.0 μm, Appl. Opt. 37 (1998) 4933–4935.
[42] A. Ćirić, S. Stojadinović, M. Sekulić, M.D. Dramićanin, JOES: An application software for Judd-Ofelt analysis from Eu3+ emission spectra, J. Lumin. 205 (2019) 351–356.